Complete Dynamics From Ignition to Stabilization of a Lean Hydrogen Flame With Thickened Flame Model

M. Amerighi, G. Senatori, A. Andreini, Thierry Schuller, Tarik Yahou, J R Dawson

COMPLETE DYNAMICS FROM IGNITION TO STABILIZATION OF A LEAN HYDROGEN FLAME WITH THICKENED FLAME MODEL

M. Amerighi*
G. Senatori
A. Andreini
Department of Industrial Engineering
University of Florence
50139, Via S.Marta 3, Florence, Italy
Email: matteo.amerighi@unifi.it

T. Schuller

Institut de Mécanique des Fluides de Toulouse, IMFT, Université de Toulouse, CNRS, Toulouse, France
Institut Universitaire de France (IUF), France

T. Yahou

Institut de Mécanique des Fluides de Toulouse, IMFT, Université de Toulouse, CNRS, Toulouse, France
Department of Energy and Process Engineering, Norwegian University of Science and Technology, Trondheim N-7491, Norway

J. R. Dawson

Department of Energy and Process Engineering, Norwegian University of Science and Technology, Trondheim N-7491, Norway

ABSTRACT

In recent years, attention has been paid to hydrogen thanks to its carbon-free nature and its interesting characteristics as an energy vector. Despite the large number of numerical analyses regarding hydrocarbon combustion in all the steady and unsteady processes, few papers that cover all those aspects are available in the literature for hydrogen flames. Therefore, a numerical methodology to explore the complete ignition sequence from the spark release to the flame stabilization is validated on a single-sector hydrogen burner. In this context, a preliminary DNS investigation of laminar spherical expanding flames is performed using different diffusive transport models to isolate their impact. The present work, carried out within the European project HESTIA, investigates the atmospheric test rig installed at the Norwegian University of Science and Technology operating with a lean, perfectly premixed, hydrogen-air flame stabilized on a conical bluff body. Four simulations are performed adopting the Thickened Flame Model with an energy deposition strategy to assess the impact of preferential and thermal diffusion, as well as grid resolution, on flame dynamics. 3D flame structure visualization coupled with detailed PIV/OH-PLIF measurements allows the investigation of the key mechanisms involved during the ignition. The dynamic response of the flame through axial fluctuations once the ignition transient is concluded, is reconstructed by the numerical strategy employed. Although the overall behavior is almost unchanged by including or not thermal diffusion effects, their local impact on the flame is evident leading to a better agreement with experimental data.

*Address all correspondence to this author.

NOMENCLATURE

D_{th}	Thermal diffusion coefficient
F	Thickening factor
L	Propagation distance
R_{spark}	Spark radius
s_l^0	Laminar flame speed
Y_i	Species mass fraction
δ_l^0	Laminar flame thickness
ϕ	Equivalence ratio
$\dot{\omega}$	Laminar reaction rate

Acronyms

AJ	Annular Jet
DNS	Direct Numerical Simulation
ED	Energy Deposition
IRZ	Inner Recirculation Zone
LES	Large Eddy Simulation
ORZ	Outer Recirculation Zone
PIV	Particle Image Velocimetry
PLIF	Planar Laser Induced Fluorescence
TFM	Thickened Flame Model
UDF	User Defined Function

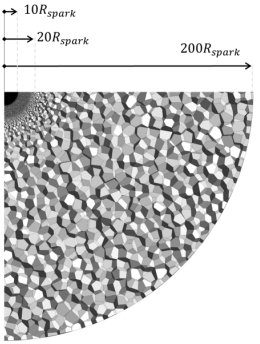

Fig. 1. 2D SECTION VIEW OF THE COMPUTATIONAL GRID EMPLOYED FOR THE SPHERICAL IGNITION SIMULATIONS WITH A SCHEMATIC REPRESENTATION OF THE REFINEMENT ZONES EXTENSION.

INTRODUCTION

The transition from fossil-based to renewable energy sources is a necessary step to reduce greenhouse gas emissions produced by human activities, responsible for climate change and global warming [1]. Nowadays, there are numerous sources contributing to the climate crisis including power generation, public transportation and industrial sector. In civil aviation, kerosene-type fuels are mostly employed although, as a consequence of the combustion process, nitrogen oxides NO_x and carbon dioxide CO_2 are obtained. In this context, hydrogen is considered one of the most promising alternatives due to its carbon-free nature [2]. However, higher adiabatic flame temperatures can lead to an increase in NO_x emissions that can be controlled by shifting the operating point towards leaner combustion.

The high reactivity and the fast diffusivity of hydrogen requires the assessment of numerical models, commonly used and tested for hydrocarbon fuels, to ensure a reliable and accurate prediction of the combustion process. Preferential and differential diffusion can affect the local flame structure and the propagation speed, particularly for lean hydrogen flames. These effects are more relevant in laminar or moderately turbulent flames until turbulent transport dominates [3].

An important parameter to describe the transport phenomena and the aforementioned effects is the Lewis number, which compares heat to mass diffusion. Preferential diffusion is related to the different diffusion velocities, and thus different species Lewis numbers of the major chemical species [4] and it may result in variations of the local stoichiometry, affecting temperature and fuel mass burning rate [5]. Differential diffusion, conversely, concerns the imbalance between heat and mass diffusivities and affects the flame response to the strain and curvature effects based on the value of the effective Lewis number of the mixture. As reported in [6], this value tends to the Lewis of the deficient species and, for a lean hydrogen-air mixture, it assumes a value close to 0.3 at ambient initial temperature and pressure. In fact, in these conditions, if the curvature of the flame front is convex towards the fresh mixture, species diffuse towards the burnt gases faster than the heat dispersion, increasing temperature and leading to an increase in the flame propagation speed [7]. Vice versa, the flame speed decreases if the curvature is convex to the burnt mixture. This can lead to so-called thermodiffusive instabilities, resulting in an enhancement of the flame front wrinkling and affecting the flame dynamics [8]. The local species composition is also altered by thermal diffusion (known in literature as Soret effect), which involves the diffusion of species due to temperature gradients, driving low (high) molecular weight species towards higher (lower) temperature zones [9].

From a numerical perspective, the calculation of these diffusive fluxes is a difficult task that requires significant computational efforts [10]. For this reason, several transport models with various levels of approximation are available in the literature. The most accurate model is the multicomponent approach, in which diffusion is considered a binary process between the different species. Conversely, the mixture-averaged approach considers the diffusion of the generic species within the mixture. These two approaches assume that the species diffusion process occurs with different velocities accounting for preferential diffusion. The simplest approach is to impose a constant Lewis number equal for each species. However, in the most extreme case, this approximation reduces to considering a unity Lewis number, preventing preferential and differential diffusion effects from being captured. The reader interested in further details can refer to [11]. Neglecting preferential diffusion and assuming a unity Lewis number for the mixture is an acceptable assumption in the case of hydrocarbons under many condi-

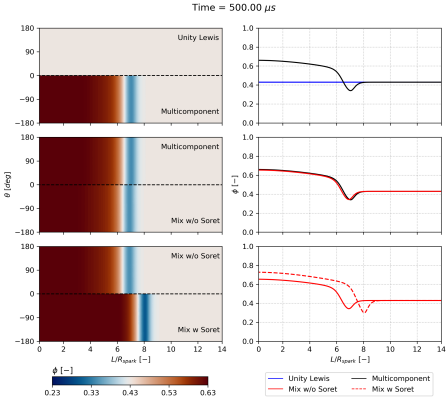

Fig. 2. CONTOURS OF EQUIVALENCE RATIO (LEFT) AND ITS TREND OVER THE BLACK DASHED LINE AS A FUNCTION OF PROPAGATION DISTANCE (RIGHT) USING DIFFERENT TRANSPORT MODELS.

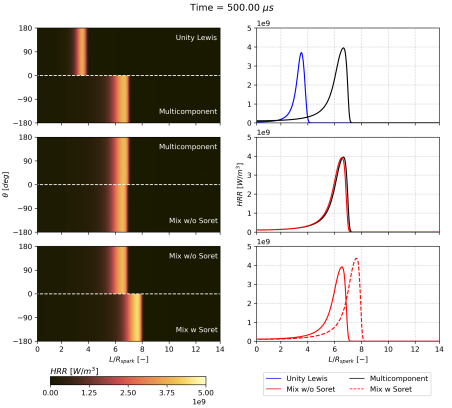

Fig. 3. CONTOURS OF HRR (LEFT) AND ITS TREND OVER THE WHITE DASHED LINE AS A FUNCTION OF PROPAGATION DISTANCE (RIGHT) USING DIFFERENT TRANSPORT MODELS.

tions [4, 12], whereas for lean hydrogen mixtures, this affects flame evolution and propagation [13]. The impact of the non-unity Lewis on the stabilization and blow-off of laminar hydrogen enriched premixed flames is presented in [14]. In [15], an evaluation of the effect of thermal diffusion on the stabilization of a premixed flame is conducted. In contrast, there is a lack of numerical works that analyze these effects on the complete dynamics from ignition to flame stabilization of hydrogen mixtures.

Therefore, the main purpose of this work is to investigate the full ignition sequence and stabilization of a lean perfectly premixed hydrogen-air flame. A preliminary analysis is conducted first by simulating spherical laminar flames using different transport models in a DNS framework, highlighting the impact of preferential and thermal diffusion. Then, a LES high-fidelity investigation adopting a species transport approach with the Thickened Flame Model is employed to simulate the academic test rig installed at the Norwegian University of Science and Technology (NTNU). The rig operates under ambient conditions and consists of a conical bluff body in which the flame stabilizes. Two main LES simulations are performed to assess a numerical setup that ensures an accurate prediction of the ignition and stabilization dynamics, considering and evaluating the different properties of hydrogen. Furthermore, two additional simulations are computed to highlight both the stochastic nature of the grid resolution and the impact of the grid resolution.

IMPACT OF DIFFUSION TRANSPORT MODELS

In this section, an analysis is carried out to evaluate the influence of preferential and thermal diffusion on the early stages of the ignition sequence and select the appropriate diffusion transport model for subsequent simulations. In particular, a laminar spherical expanding flame is simulated with the commercial software ANSYS Fluent® 2022R1 through a DNS approach. The 3D spherical domain has a radius of 50 mm and the computational grid consists of 12.4 millions of polyhedral elements with different levels of refinement, as shown in Fig. 1. The inner part within ten times the spark radius has a grid size of 20 μm, while the elements in the outer part are characterized by a dimension of 5 mm in order to reduce the computational cost and damp potential pressure wave reflections. The intermediate refinement is required to provide a smooth transition between the fine and the coarse grid. During the calculation, the flame remains confined within the inner refinement region, ensuring the correct discretization. It is important to underline that cellular instabilities are not observed, as shown below, since the critical radius [16] is not reached to limit computational efforts and the study of these effects is beyond the scope of this part. All DNS are performed using the pressure-based solver, the coupled algorithm for the pressure-velocity coupling and the Boivin reaction mechanism [17], which consists of 9 species and 12 reactions. A constant time step of $1 \cdot 10^{-7}$ s is used. The atmospheric pressure is prescribed at the outlet patch. Initially, the domain is filled with a homogeneous hydrogen-air mixture at 298 K characterized by an equivalence ratio of 0.43, i.e. the same operating conditions of the test case under investigation. Subsequently, ignition occurs in the quiescent mixture at the center of the spherical domain using the Energy Deposition (ED) model [18], implemented in the software through a User Defined Function (UDF). The spark has a characteristic radius R_{spark} of 250 μm, a duration of 80 μs and the energy deposited is 0.025 mJ.

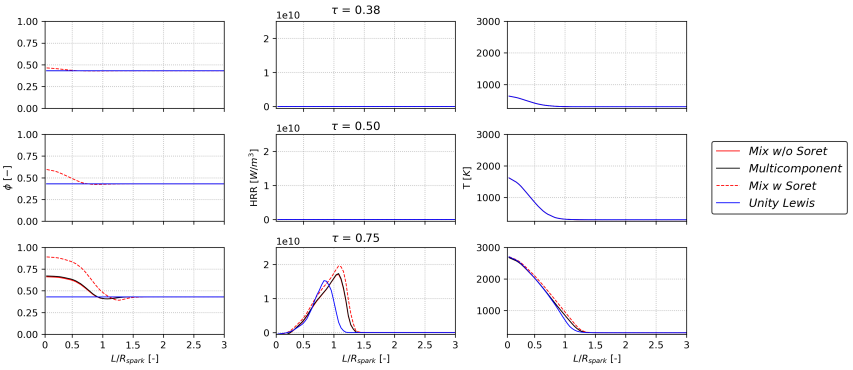

Fig. 4. EQUIVALENCE RATIO, HEAT RELEASE RATE, AND TEMPERATURE AS FUNCTIONS OF PROPAGATION DISTANCE AND TIME USING DIFFERENT TRANSPORT MODELS: MULTICOMPONENT, MIXTURE-AVERAGED, UNITY-LEWIS ASSUMPTION, AND MIXTURE-AVERAGED WITH SORET EFFECT.

Four different simulations are performed by using the same operating conditions, equivalence ratio, computational grid and time step. However, the transport model is modified in order to investigate the influence of preferential diffusion and Soret effect on the early stages of the ignition process. In particular, the multicomponent approach, the mixture-averaged model with and without the Soret effect and the unity-Lewis assumption are compared.

To analyze the differences between the various approaches it is useful to refer to Fig. 2 and Fig. 3 which provide the instantaneous contours of the equivalence ratio ϕ and the Heat Release Rate (HRR) with the purpose of representing the curved flame front in a straight configuration. The plots on the right side of these figures show the trend of the mentioned quantities as a function of the propagation distance L normalized with the spark radius R_{spark}. It is important to underline that the equivalence ratio is evaluated using Bilger's formulation [19], which is based on the elemental mass fraction. With the unity-Lewis assumption, preferential diffusion is ignored and the perfectly premixed mixture exhibits a constant equivalence ratio, equal to the nominal one, in the entire domain. Contrarily, with the multicomponent model it is possible to observe a decrease in the equivalence ratio on the fresh mixture side due to the high diffusivity of hydrogen. Furthermore, as a consequence of the positive curvature, a greater amount of reactants at the flame front leads to an increase in HRR. This is related both to the rise in temperature, which affects the propagation speed, and to the effect that stretch has on a mixture with a Lewis number lower than one. The result is that at the same instant, the HRR peak obtained with the multicomponent transport model is shifted towards higher L/R_{spark} compared to the one retrieved with the unity-Lewis assumption, indicating a greater flame propagation speed. The results of the mixture-averaged approach are consistent and comparable with those obtained with the multicomponent and thus it is selected to investigate the role of the Soret effect. Thermal diffusion amplifies the mentioned effects resulting in a richer mixture passing through the flame front and, therefore, in a further increase in HRR. The comprehension of this phenomenon can be enhanced by analyzing Fig. 4, in which the equivalence ratio, the HRR and the temperature are shown as functions of the L/R_{spark} ratio and τ, i.e. the time normalized with the duration of the spark. It is possible to notice that for $\tau = 0.38$, the temperature rise induced by the spark involves, when the Soret is enabled, the migration of hydrogen towards the center of the spark, resulting in a rise of ϕ in this region. The reactions are not triggered, as evidenced by the fact that the HRR is zero. At $\tau = 0.5$, the aforementioned effect is amplified due to the further increase in temperature and ϕ reaches a value of 0.6. This implies that until reactions occur, only the model involving thermal diffusion exhibits a change in ϕ. Conversely, the phenomenon of preferential diffusion is relevant when the combustion begins to progress ($\tau > 0.65$) resulting in a concentration gradient that determines the species diffusion towards the flame front and a significant variation of ϕ.

In conclusion, the unity-Lewis assumption underestimates the flame propagation speed. The results obtained using the mixture-averaged approach are comparable to those achieved with multicomponent, and the thermal diffusion leads to a further increase in HRR and flame propagation speed. Therefore, the mixture-averaged transport model is selected for the subsequent investigations, allowing for a good compromise between accuracy and computational cost. Furthermore, to provide an additional sensitivity, calculations are conducted with and without the Soret effect.

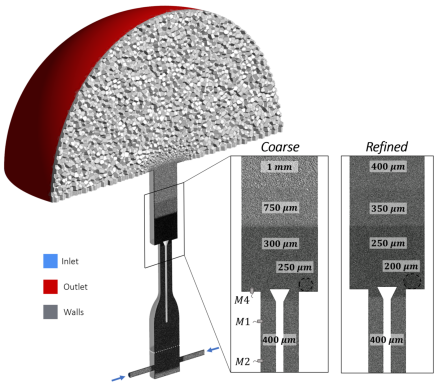

Fig. 5. COMPUTATIONAL DOMAIN WITH THE PRESCRIBED BOUNDARY CONDITIONS. THE TWO GRIDS EMPLOYED, INCLUDING REFINEMENT ZONES, ARE HIGHLIGHTED WITH A SCHEMATIC REPRESENTATION OF THE PROBES INSTALLED IN THE EXPERIMENTAL RIG.

	Operating conditions
Mixture	Perfectly premixed
Fuel	100% H_2
Equivalence ratio	0.43
Operating pressure	101325 Pa
Inlet temperature	298 K
Bulk velocity	$5 m.s^{-1}$

Table 1. OPERATING CONDITIONS OF THE TEST RIG.

Name	**Mixture**	**Time-step**	**Soret**	**Mesh**
NR	*Air*	$1 \cdot 10^{-5} s$	–	Coarse
R1	H_2-air	$5 \cdot 10^{-6} s$	×	Coarse
R2	H_2-air	$5 \cdot 10^{-6} s$	×	Coarse
R3S	H_2-air	$5 \cdot 10^{-6} s$	✓	Coarse
R4S	H_2-air	$5 \cdot 10^{-6} s$	✓	Refined

Table 2. DESCRIPTION OF THE SIMULATION CASES

.

EXPERIMENTAL RIG AND COMPUTATIONAL DOMAIN

A schematic representation of the atmospheric test rig analyzed in this work is shown in Fig. 5. The mixture is supplied by two opposite inlets at the bottom part of the rig and a grid with appropriate spacing is placed downstream of the jets in order to uniform the turbulence intensity and length scales. Along the center of the duct, a rod holds the conical bluff body, used to stabilize the flame. A pure air mixture is used for the non-reactive tests, whereas a perfectly premixed hydrogen-air mixture at $\phi = 0.43$ is employed in the reactive conditions. In both cases, the mixture is supplied at the ambient temperature of 298 K with a mass flow rate that allows to obtain a bulk velocity of 5 m.s^{-1} in the constant section duct upstream the combustion chamber. A complete summary of the operating conditions of the test rig is reported in Table 1.

During the experimental tests, the pressure inside the combustion chamber and in the duct is measured with the probes labeled M4, M1 and M2 in Fig. 5. Furthermore, the Particle Image Velocimetry (PIV) technique is used to acquire the flow field in non-reactive conditions and it is time-synchronized with the OH-Planar Laser Induced Fluorescence (OH-PLIF) system during the ignition process until the complete flame stabilization. A detailed description of the test rig, experimental procedure, and measurement techniques can be found in [20, 21].

The plenum, the two opposite inlets and the combustion chamber are included in the computational domain, in order to avoid any modifications of the acoustic of the system and ensure consistency with the experimental test rig. Furthermore, an external hemisphere is included at the outlet to mimic the discharge into the atmosphere and prevent acoustic wave reflections.

Two different unstructured grids are adopted, both based on polyhedral elements, as shown in Fig. 5. A *coarse* and *refined* strategies, counting 21 and 34 million elements respectively, are tested in order to investigate the impact of the spatial resolution on the ignition dynamics. In both cases, the dimension of the elements within the stabilization zone is maintained below 300 μm with an additional spherical refinement at the spark position in order to properly capture the kernel evolution during the initial steps after the spark. Towards the outlet section, the sizing gradually increases to 1 mm and 400 μm for, respectively, the *coarse* and *refined* mesh. To prevent excessive numerical dissipation of the turbulence generated by the opposite jets, the grid cell size between the plenum and burner exit is kept at 400 μm.

NUMERICAL SETUP

A non-reactive LES simulation with only air (named NR) is initially performed to validate the cold flow field. Subsequently, starting from a cold hydrogen-air LES simulation, the ignition process is modeled (R1 to R4S) until the stable flame condition is reached. Then, the solutions are averaged in order to obtain the reactive time-statistic results to compare with the available experimental data. A summary of the simulations performed and their main parameters is reported in Table 2. In particular, two reactive simulations (R1 and R2), are conducted under the same operating conditions and with the same computational grid (*coarse*) to highlight the stochastic nature of the process. Subsequently, the R3S simulation is introduced to investigate the role of the Soret

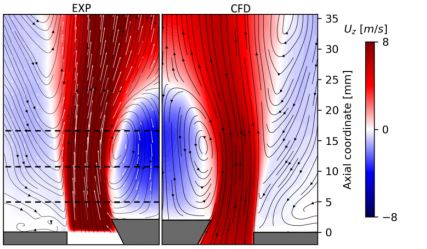

Fig. 6. EXPERIMENTAL (LEFT) AND NUMERICAL (RIGHT) TIME-AVERAGED AXIAL VELOCITY FIELD.

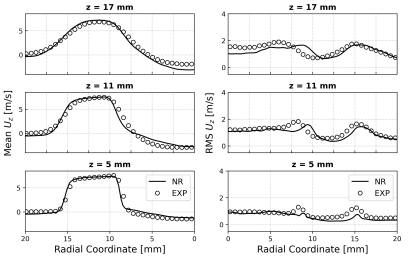

Fig. 7. COMPARISON BETWEEN NUMERICAL AND EXPERIMENTAL DATA AT DIFFERENT STREAMWISE LOCATIONS IN TERMS OF TIME-AVERAGED (LEFT) AND RMS OF AXIAL VELOCITY (RIGHT).

effect. Finally, the R4S simulation is carried out with the *refined* mesh to assess the impact of the spatial resolution.

A constant inlet mass flow rate, which allows to achieve a bulk velocity of 5 m.s^{-1} in the duct upstream of the chamber, is imposed at both inlet patches of the opposite jets. The flow enters with a temperature of 298 K and, in the reactive simulations, has an equivalence ratio of 0.43. The solid walls are treated as adiabatic, with the exception of the bluff body, which is maintained at a constant temperature of 470 K in all the reactive simulations, in accordance with the experimental procedure. A non-slip condition is also imposed. The atmospheric pressure is set at the outlet patch, whereas an air co-flow with a low velocity is imposed at the hemisphere inlet. The Dynamic Smagorinsky-Lilly model [22] is used in all the simulations to model the effect of unresolved eddies. The turbulence chemistry interaction is handled with the Thickened Flame Model [23]. This approach is based on the idea that the resolution of the flame front, due to its reduced thickness, is unaffordable in the common numerical grid employed in LES calculations. Therefore, the aim is to artificially thicken the flame front to make its resolution possible. This objective is achieved by altering the reaction rate $\dot{\omega}$ and thermal diffusivity D_{th}, using a thickening factor F>1, as follows:

$$\delta_l^0 \propto \sqrt{\frac{D_{th}}{\dot{\omega}}} \rightarrow \delta_l^1 \propto \sqrt{\frac{FD_{th}}{\dot{\omega}/F}} = F\sqrt{\frac{D_{th}}{\dot{\omega}}} = F\delta_l^0 \quad (1)$$

$$s_l^0 \propto \sqrt{D_{th}\dot{\omega}} \rightarrow s_l^1 \propto \sqrt{FD_{th}\frac{\dot{\omega}}{F}} = \sqrt{D_{th}\dot{\omega}} = s_l^0 \quad (2)$$

where the superscripts 0 and 1 refer to the unthickened and thickened flame respectively. As a result of this procedure, the laminar flame speed s_l^0, which affects the stabilization and the position of the flame, is preserved while the flame thickness is increased by factor F. Nevertheless, the thickening of the flame front alters the interaction between turbulence and chemistry, resulting in a reduction of the flame surface and thus, the reaction rate. To compensate for this effect, an efficiency function E is used.

In the present work, a constant thickening factor F equal to 4 is imposed via UDF, ensuring a proper flame discretization in the whole domain [24], especially for the *refined* strategy. The efficiency function proposed by Colin [23], also implemented via UDF, is used to restore the interaction between turbulence and chemistry. The skeletal Boivin reaction mechanism and the mixture-averaged approach are selected as a result of the preliminary analysis of spherical expanding flames. The spark is modeled with the ED model implemented via UDF. The deposited energy is equal to 11 mJ and corresponds to 30% of the energy supplied experimentally. This strategy permits to account for the thermal conduction to the electrodes, radiation, and shock wave expansion that reduce the actual transmitted energy [18, 25]. In order to maintain the temperature at the spark center below 3000 K, a characteristic spark size of 5.5 mm and a duration of 100 µs are selected. In accordance with the experimental setup, the spark is placed in an xz-plane at a distance of 20 mm from the chamber axis and 3 mm from the back plate. The simulations are carried out with a pressure-based solver and the SIMPLEC algorithm is used for the pressure-velocity coupling. Second-order upwind schemes are employed for the spatial discretization and the temporal formulation is realized with a bounded second-order implicit scheme. A constant time step of $1 \cdot 10^{-5}$ s is used in the non-reactive case, whereas in the reactive simulations it is reduced to $5 \cdot 10^{-6}$ s in order to ensure a proper resolution of the chemistry.

RESULTS

In the first part of this section, the non-reactive flow field is examined due to its significant impact on the flame evolution. Subsequently, the ignition sequence and the stable flame conditions are investigated through a comprehensive comparison with the experimental data.

Cold flow field

The cold flow field structure is evaluated by examining the numerical and the experimental time-averaged axial

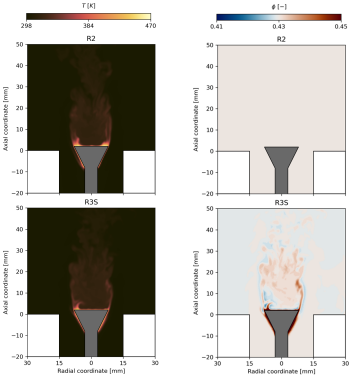

Fig. 8. INSTANTANEOUS CONTOURS OF TEMPERATURE AND EQUIVALENCE RATIO FOR R2 (TOP ROW) AND R3S (BOTTOM ROW).

velocity maps, as represented in Fig. 6. In fact, in accordance with the geometry and the absence of any significant sources of tangential or radial components, the axial velocity is predominant. The numerical prediction exhibits an overall remarkable agreement with the experimental results. The streamwise extension of the Inner Recirculation Zone (IRZ) is accurately reproduced and both the Outer Recirculation Zone (ORZ) and the Annular Jet (AJ) are consistent in terms of configuration and intensity.

In order to achieve a more accurate evaluation, the time-averaged (left) and the RMS (right) of the axial velocity profiles, measured at different locations above the chamber backplate and indicated by the black dashed lines in Fig. 6, are compared with those obtained experimentally by employing the PIV technique in Fig. 7. The comparison confirms the correct prediction of the mean velocity, particularly at low axial coordinates (5 and 11 mm) where the results are almost matched. The peak of the velocity in the AJ is well captured, even if the intensity of the IRZ is underestimated along the burner axis. The RMS profiles of the axial velocity reveal a slight underestimation at all locations, although the trend is comparable and in line with the experimental results. This is probably related to the numerical dissipation of the turbulence downstream of the perforated grid inside the plenum. In fact, although the grid size is maintained constant at 400 µm for the entire axial extension of this zone (approximately 250 mm), it may not be sufficient to retrieve the proper value inside the chamber. In this context, several previous LES simulations were performed to investigate the impact of different levels of mesh refinement upstream the combustion chamber or injection strategies. However, the aforementioned approach is selected as it respects the Celik criterion [26] and provides satisfactory values of turbulent fluctuations while maintaining a reasonable computational cost.

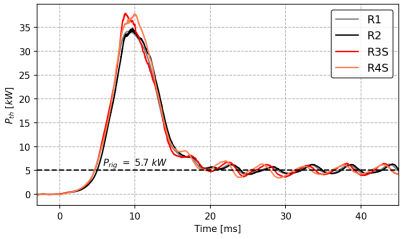

Fig. 9. THERMAL POWER AS A FUNCTION OF TIME FOR R1, R2, R3S AND R4S. THE NOMINAL THERMAL POWER IS REPRESENTED BY THE GREY DASHED LINE.

From ignition to flame stabilization

Prior to introducing the ignition dynamic and the comparison with the experimental data, it is important to examine the cold flow fields at the instant of the spark release (t = 0 ms), before the triggering of reactions, in order to isolate the effect of thermal diffusion. In fact, when the combustion process takes place, the Soret effect is enhanced by greater temperature gradients and the occurrence of preferential diffusion effects leads to a challenging identification. To clearly visualize the impact of the Soret effect, it is useful to refer to Fig. 8, which provides the instantaneous temperature and equivalence ratio fields for R2 (top row) and R3S (bottom row). Although both simulations show a temperature gradient in the IRZ due to the preheating of the bluff body, de-mixing effects are only observed in R3S with the formation of rich and lean spots with respect to the nominal value of 0.43. However, the impact of this effect is limited, as evidenced by the narrow range of the ϕ contours, because the magnitude of the temperature gradients is small. Finally, it is important to note that these effects mainly occur in the IRZ, while the outer recirculation zone remains almost unaffected. On the contrary, in R2 a uniform equivalence ratio field is present in the entire domain.

When the energy required to ignite the mixture is released, reactions occur and the ignition transient proceeds until the flame stabilizes on the bluff body. A fundamental parameter that must be considered is the thermal power of the rig, calculated in the numerical simulations as the volume integral of the HRR. The time-series behavior is reported in Fig. 9, in which it is possible to observe that the complete ignition of the chamber is achieved in approximately 23 ms. In fact, when stable conditions are reached, the power oscillates around the nominal value ($P_{rig} \approx$ 5.7 kW), determined by the product of the fuel mass flow rate and the lower heating value of hydrogen. The first conclusion that can be drawn by comparing R1 and R2 is related to the stochasticity of the ignition process due to the nature of the turbulence. Indeed, these simulations are conducted with the same mesh and setup and the only difference is represented by the time at which the spark is released and thus, the local flow field. Due to the low turbulence levels of the rig (Re$\approx$7000), the

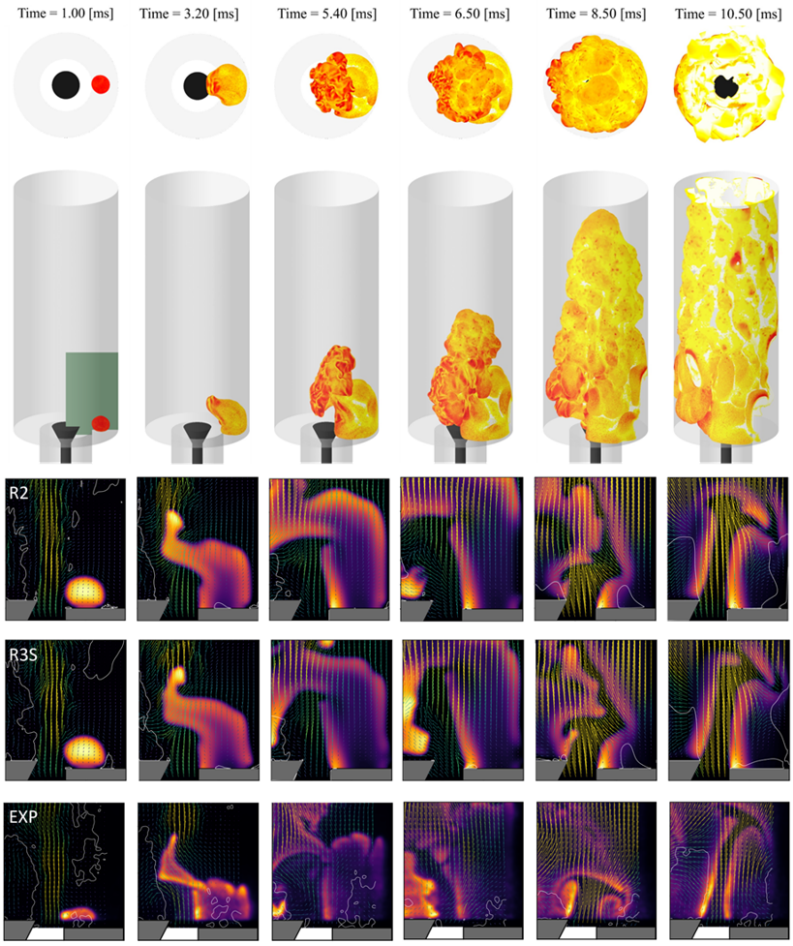

Fig. 10. 3D FLAME VISUALIZATION USING AN ISOSURFACE OF HRR (10^8 W/m^3) COLORED BY TEMPERATURE FOR R2 (TOP PART OF IMAGE). INSTANTANEOUS CONTOURS OF NORMALIZED OH MASS FRACTION WITH OVERLAPPED VELOCITY VECTORS AND WHITE ISOLINES OF ZERO AXIAL VELOCITY REPRESENTED IN THE HIGHLIGHTED LIGHT-GREEN PLANE (BOTTOM PART OF IMAGE). NUMERICAL RESULTS OF R2 (TOP ROW), R3S (CENTRAL ROW), AND EXPERIMENTAL PIV/OH-PLIF DATA (BOTTOM ROW).

signals exhibit a similar global trend, although local variations are present. However, with the inclusion of the Soret effect (R3S and R4S), it is possible to notice a slightly faster ignition, underlined by the shift of the curves towards lower times, and a higher maximum power. These effects are attributed to the local increase in fuel mass fraction at the flame front, which enhances the flame speed, as previously pointed out.

The crucial temporal instants of the ignition sequence are reported in the top part of Fig. 10 through two visualizations (top and isometric view) of an isosurface of HHR (10^8 W/m^3) colored by temperature. The 3D flame images are reported only for the R2 case for the sake of brevity. Furthermore, in the bottom part of Fig. 10, the results of R2

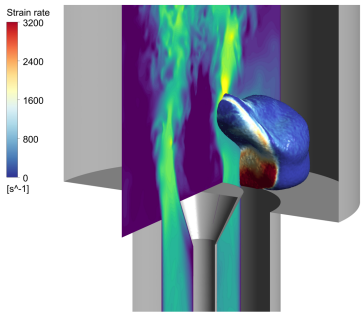

Fig. 11. INSTANTANEOUS CONTOUR OF AXIAL VELOCITY ON A LONGITUDINAL PLANE WITH AN ISOSURFACE OF HRR (10^8 W/m^3) COLORED BY LOCAL STRAIN RATE VALUES FOR R2 CASE.

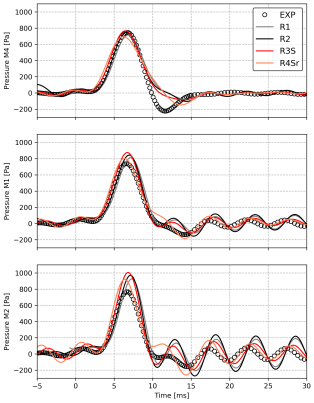

Fig. 12. PRESSURE SIGNAL MEASURED AT THE CHAMBER BACK PLATE (M4) AND INSIDE THE DUCT (M1 AND M2). BOTH NUMERICAL (R1, R2, R3S AND R4S) AND EXPERIMENTAL RESULTS ARE FILTERED AT 200 Hz.

and R3S are compared with the instantaneous experimental images obtained using PIV coupled with OH-PLIF also permitting to assess the impact of the Soret effect.

The spark release leads to the formation of a spherical kernel that grows and propagates in the ORZ due to the favorable conditions of the flow field. At t = 3.2 ms, the phase of jet-flame interaction is depicted. A lack of penetration near the edge of the back plate can be observed, which is related to the presence of high strain values, leading to local extinctions and forcing the flame to propagate in different directions. This aspect can be appreciated in more detail by referring to Fig. 11, which shows an instantaneous contour of the axial velocity on a longitudinal plane with an isosurface of HRR (10^8 W/m^3) colored by local strain rate, calculated as the derivative of the axial velocity with respect to the radial direction for R2 case. It can be observed that when the strain rate exceeds the extinction value, which is estimated to be 3200 s^{-1} under these operating conditions [27], the flame is not able to penetrate the shear layer. In fact, only when downstream regions are reached, the penetration of the annular jet and the approach of the IRZ can occur (t = 5.4 ms). To complete the ignition of the chamber, the flame propagates and anchors in the ORZ (t = 6.5 - 10 ms), until its stabilization on the bluff body. No significant differences can be observed between the two simulations. However, the flame timing in approaching the IRZ predicted by R2 at t = 5.4 and t = 6.5 ms is delayed compared to that provided by the experiments and R3S, in accordance with the previous considerations in terms of thermal power. Despite the agreement with the experimental data confirmed in terms of penetration length and flame dynamics, it is important to highlight that only a single run is analyzed for both CFD and experimental data in Fig. 10. Therefore, to demonstrate the reliability of the numerical results and to provide a quantitative comparison, the pressure signal recorded in the chamber (M4) and in the duct (M1 and M2) is evaluated in Fig. 12. The experimental time-series are averaged over a minimum of 8 tests and are low-pass filtered at 200 Hz. The same filtering procedure is applied to the numerical results that are each representative of a single run, as previously highlighted.

Considering the M4 signal, it can be noted that when the spark is released (t = 0 ms), the pressure is almost constant. The increase in temperature and the thermal expansion of the burnt mixture cause a rise in the chamber pressure, inducing the gases to accelerate towards the outlet. This results in a rapid drop in pressure until the negative peak is reached (t $\approx$ 11 ms). When a stable condition is achieved, the pressure oscillates around the initial value with a certain frequency of 180 Hz. The overpressure is accurately predicted by all the simulations in terms of magnitude and time shift with respect to the spark time. In fact, the rate of pressure increase/decrease is in good agreement with the experimental data until approximately 10 ms. Then, mainly for the *coarse* mesh simulations, the negative pressure peak exhibits a lower value and time delay compared to the experimental results. The same conclusions can be drawn for M1 and M2 signals, in which a slight overestimation of the pressure peaks is observed. Nevertheless, it is demonstrated that the inclusion of the Soret effect results in more consistent agreement with experimental data. This is particularly evident when the flame reaches stable conditions, where the pressure oscillations are well reproduced in terms of frequency and amplitude. For these reasons, the simulation with the *refined* mesh and the Soret effect (R4S) is carried out permitting to better discretize the exhaust gas acceleration, resulting in a further improvement of the time signals at all locations.

To investigate the effect of thermal diffusion in more detail, Fig. 13 reports the numerical instantaneous fields of equivalence ratio, HRR, mass fraction of radical H and temperature. For a proper analysis with a consistent setup (e.g.

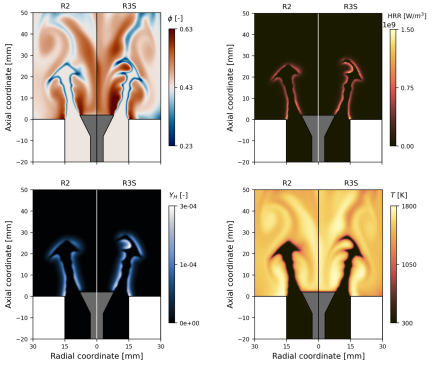

Fig. 13. INSTANTANEOUS CONTOURS OF EQUIVALENCE RATIO, HEAT RELEASE RATE, MASS FRACTION OF THE RADICAL H, AND TEMPERATURE FIELD FOR R2 AND R3S.

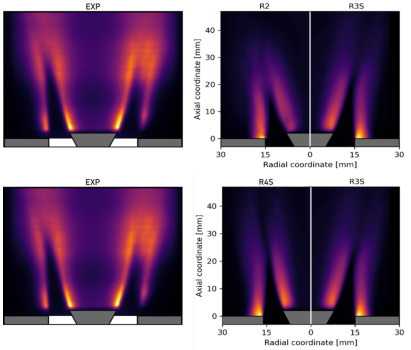

Fig. 14. MEAN FLAME IMAGES OBTAINED WITH THE OH-PLIF TECHNIQUE (LEFT) AND CONTOURS OF TIME-AVERAGED OH MASS FRACTION FOR R2, R3S AND R4S (RIGHT), NORMALIZED WITH THE RELATIVE MAXIMUM VALUE.

same computational grid), the comparison considers only R2 and R3S. As shown in the equivalence ratio contour, the redistribution caused by preferential diffusion is amplified in R3S due to the Soret effect. In particular, no significant differences appear between the two cases at the outer flame branch. However, at the inner one, the mixture is richer due to the effect of the thermostated bluff body and the consequent higher temperature gradient involved in the combustion process, which draw more hydrogen towards the flame front. Furthermore, the greater diffusion velocity of the radical H at the inner branch is highlighted in the first contour of the bottom row. Indeed, a higher concentration is predicted in all the zones characterized by a positive curvature, in agreement with the aforementioned theoretical considerations. These effects result in higher local HRR and temperatures when thermal diffusion is considered, as shown in the right side of Fig. 13.

Stable flame

Finally, when stable conditions in terms of pressure, velocity and heat release rate are reached, the anchoring process of the flame on the burner can be considered completed and the stable flame is investigated.

A comparison with the experimental data is reported in Fig. 14, in which the OH-PLIF averaged images is compared with the numerical results obtained by evaluating the mean OH mass fraction in a longitudinal plane. The experimental contour shows horizontal bands with different light intensities related to the laser intensity distribution.

Furthermore, the experimental data are not accessible in proximity to the back plate wall. Since experimental and numerical images are normalized with respect to their relative maximum values, only a qualitative comparison in terms of mean flame shape is carried out. Nevertheless, the M-shaped flame that characterizes these operating conditions is correctly predicted by all the simulations, also in terms of length, confirming the good consistency of the turbulence levels entering the chamber. The numerical prediction of R2 and R3S exhibits an OH peak at the outer shear layer, according to the higher stretch values in these regions, where the flame is attached at the back plate due to the adiabatic treatment imposed. However, the heat losses generated by the finite wall temperature of the bluff body cause a local quenching and the consequent lift-off of the flame on the inner shear layer according to the experimental map. Furthermore, the inclusion of the Soret effect in R3S determines a local peak of reactivity also in these regions, confirming its local impact. These considerations are also evident in the R4S results, which suggest that the use of a refined mesh does not significantly affect the time-average behavior.

To conclude the analysis, during stable conditions the flame oscillates in the axial direction due to the acoustic response of the rig after the ignition. Flame images obtained in the experimental context through the OH-PLIF technique (center) and the numerical contours of the normalized OH mass fraction on a longitudinal plane for R3S (left) and R4S (right) are reported in Fig. 15 for a complete oscillation period. It is possible to observe that at t = 20 ms the flame has a shorter length resulting in a reduction in the flame front surface and therefore in the thermal power, in accordance with the results shown in Fig. 9. Conversely, the flame surface and the thermal power increase at approximately 23 ms, where the flame length is greater. The oscillations are accurately predicted in terms of shape and length of the flame and in terms of frequency, confirming the reliability of the numerical models employed.

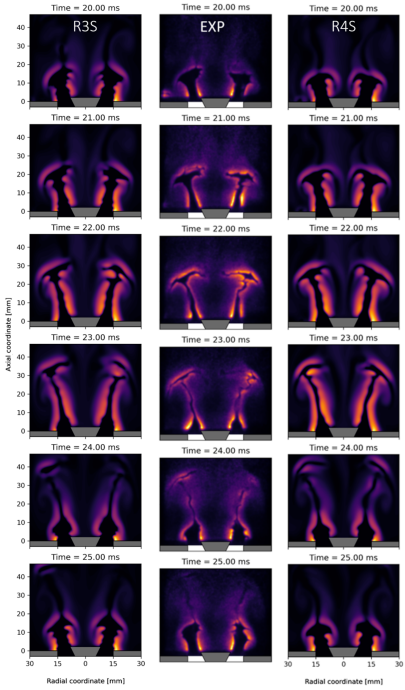

Fig. 15. INSTANTANEOUS FLAME IMAGES OBTAINED WITH THE OH-PLIF (CENTER) AND INSTANTANEOUS CONTOURS OF THE NORMALIZED OH MASS FRACTION ON A LONGITUDINAL PLANE FOR R3S (LEFT) AND R4S (RIGHT) FOR DIFFERENT INSTANTS OF TIME.

CONCLUSION

The main purpose of this work is to investigate the impact of diffusion transport models on the ignition transient of a lean perfectly premixed hydrogen flame, starting from the cold flow field to the complete flame stabilization. In order to assess the impact of transport models on the early stages of ignition, spherical laminar expanding flames are simulated using a DNS approach. The study confirms that the unity-Lewis assumption results in an underestimation of both HRR and flame propagation speed, in contrast to the more accurate multicomponent model which accounts for preferential and differential diffusion effects. Since the mixture-averaged approach accurately captures these phenomena, it is selected for the subsequent analysis.

The test rig investigated operates under ambient conditions in terms of pressure and temperature. Firstly, the validation of the cold flow field is conducted using pure air. In this context, several sensitivities are performed to identify optimal elements grid size and computational domain strategy as a compromise between the accuracy of the results and the computational effort. Two reactive LES simulations (R1 and R2) are performed under the same operating conditions and numerical setup to investigate the stochasticity of the ignition process. Then, R3S and R4S simulations are presented to analyze the effect of thermal diffusion and spatial grid resolution respectively.

It is observed that even in the absence of reactions, the Soret effect affects the local composition of the mixture, resulting in a redistribution of species and local de-mixing. When the spark is released, the ignition process is analyzed until the flame stabilization on the bluff body. The ignition sequence is accurately predicted in terms of timing and flame evolution as confirmed by the comparison with experimental data averaged over several tests, underlining the reliability of the numerical simulations. Although the dynamics of ignition and flame development do not show significant differences between the R2 and R3S, the inclusion of thermal diffusion results in a slightly faster ignition with a higher thermal power peak, related to the presence of locally richer zones that leads to a local increase in HRR and temperature. However, for a more accurate reconstruction of pressure signals and flame evolution, it is demonstrated that a refined sizing is requested. Finally, the stable flame is analyzed. The height and M-shape of the flame are correctly predicted and it is shown that the Soret effect mainly influences the inner branch of the flame, due to its proximity to the IRZ and the thermostated bluff body.

In conclusion, the excellent agreement with the experimental data confirms the reliability of the numerical setup employed for the prediction of both the ignition transient and stable flame conditions. The results suggest that the Soret effect has a minor impact on ignition dynamics and global behavior, whereas it plays an important role concerning local flame phenomena and characteristics.

Acknowledgements

This project HESTIA has received funding from the European Union Horizon Europe research and Innovation program under Grant Agreement No. 101056865.

References

[1] Öberg, S., Odenberger, M., and Johnsson, F., 2022. "Exploring the competitiveness of hydrogen-fueled gas turbines in future energy systems". *International Journal of Hydrogen Energy,* **47**, pp. 624–644.

[2] Hanglind, F., Hasselrot, A., and Singh, R., 2006. "Potential of reducing the environmental impact of aviation by using hydrogen. part i: Background, prospect and challenges". *The Aeronautical Journal*, pp. 533–540.

[3] Barlow, R. S., Dunn, M. J., Sweeney, M. S., and Hochgreb, S., 2012. "Effects of preferential transport in turbulent bluff-body-stabilized lean premixed ch4/air flames". *Combustion and Flame,* **159**(8), pp. 2563–2575.

[4] Swart, J. A. M. D., Bastiaans, R. J. M., Oijen, J. A. V., Goey, L. P. H. D., and Cant, R. S., 2010. "Inclusion of preferential diffusion in simulations of premixed combustion of hydrogen/methane mixtures with flamelet generated manifolds". *Flow, Turbulence and Combustion,* **85**, 12, pp. 473–511.

[5] Ranga Dinesh, K., Shalaby, H., Luo, K., van Oijen, J., and Thévenin, D., 2016. "High hydrogen content syngas fuel burning in lean premixed spherical flames at elevated pressures: Effects of preferential diffusion". *International Journal of Hydrogen Energy,* **41**(40), pp. 18231–18249.

[6] Matalon, M., CUI , C., and Bechtold, J., 2003. "Hydrodynamic theory of premixed flames: Effects of stoichiometry, variable transport coefficients and arbitrary reaction orders". *Journal of Fluid Mechanics,* **487**, 06, pp. 179 – 210.

[7] Poinsot, T., and Veynante, D., 2005. "Theoretical and numerical combustion". *Prog. Energy Combust. Sci.,* **28**, 01.

[8] Berger, L., Grinberg, M., Jürgens, B., Lapenna, P. E., Creta, F., Attili, A., and Pitsch, H., 2023. "Flame fingers and interactions of hydrodynamic and thermodiffusive instabilities in laminar lean hydrogen flames". *Proceedings of the Combustion Institute,* **39**(2), pp. 1525–1534.

[9] Yang, F., Law, C., Sung, C., and Zhang, H., 2010. "A mechanistic study of soret diffusion in hydrogen–air flames". *Combustion and Flame,* **157**(1), pp. 192–200.

[10] Hilbert, R., Tap, F., El-Rabii, H., and Thévenin, D., 2004. "Impact of detailed chemistry and transport models on turbulent combustion simulations". *Progress in Energy and Combustion Science,* **30**(1), pp. 61–117.

[11] Giacomazzi, E., Picchia, F., and Arcidiacono, N., 2007. "A review of chemical diffusion: Criticism and limits of simplified methods for diffusion coefficient calculation". *Combustion Theory and Modelling,* **12**, 02, pp. 135–158.

[12] Oijen, J. A. V., Donini, A., Bastiaans, R. J., ten Thije Boonkkamp, J. H., and de Goey, L. P., 2016. "State-of-the-art in premixed combustion modeling using flamelet generated manifolds". *Progress in Energy and Combustion Science,* **57**, 11, pp. 30–74.

[13] Sánchez, A. L., and Williams, F. A., 2014. "Recent advances in understanding of flammability characteristics of hydrogen". *Progress in Energy and Combustion Science,* **41**(1), pp. 1–55.

[14] Vance, F. H., Shoshin, Y., Oijen, J. A. V., and Goey, L. P. D., 2019. "Effect of lewis number on premixed laminar lean-limit flames stabilized on a bluff body". *Proceedings of the Combustion Institute,* **37**, pp. 1663–1672.

[15] Vance, F. H., de Goey, P., and van Oijen, J. A., 2020. "The effect of thermal diffusion on stabilization of premixed flames". *Combustion and Flame,* **216**, 6, pp. 45–57.

[16] Beeckmann, J., Hesse, R., Kruse, S., Berens, A., Peters, N., Pitsch, H., and Matalon, M., 2017. "Propagation speed and stability of spherically expanding hydrogen/air flames: Experimental study and asymptotics". *Proceedings of the Combustion Institute,* **36**, pp. 1531–1538.

[17] Boivin, P., Sánchez, A. L., and Williams, F. A., 2013. "Four-step and three-step systematically reduced chemistry for wide-range H2–air combustion problems". *Combust. Flame,* **160**(1), pp. 76–82.

[18] Lacaze, G., Richardson, E., and Poinsot, T., 2009. "Large eddy simulation of spark ignition in a turbulent methane jet". *Combust. Flame,* **156**(10), pp. 1993–2009.

[19] Bilger, R., 1989. "The structure of turbulent nonpremixed flames". *Symposium (International) on Combustion,* **22**(1), pp. 475–488.

[20] Yahou, T., Dawson, J. R., and Schuller, T., 2023. "Impact of chamber back pressure on the ignition dynamics of hydrogen enriched premixed flames". *Proceedings of the Combustion Institute,* **39**, 1, pp. 4641–4650.

[21] Yahou, T., Schuller, T., and Dawson, J. R., 2023. "The Effect of Ignition Procedure on Flashback of Hydrogen-Enriched Flames". *Journal of Engineering for Gas Turbines and Power,* **146**(1).

[22] Lilly, D. K., 1992. "A proposed modification of the germano subgrid-scale closure method". *Phys. Fluids A,* **4**.

[23] Colin, O., Ducros, F., Veynante, D., and Poinsot, T., 2000. "A thickened flame model for large eddy simulations of turbulent premixed combustion". *Physics of Fluids,* **12**, pp. 1843–1863.

[24] Rochette, B., Collin-Bastiani, F., Gicquel, L., Vermorel, O., Veynante, D., and Poinsot, T., 2018. "Influence of chemical schemes, numerical method and dynamic turbulent combustion modeling on les of premixed turbulent flames". *Combust. Flame,* **191**, pp. 417–430.

[25] Vogel, M., and Maly, R., 1978. "Initiation and propagation of flame fronts in lean ch4-air mixtures by the three modes of the ignition spark". *Proc. of the 17th Symp. (Int.) on Combustion, The Combustion Institute*, pp. 821–831.

[26] Celik, I. B., Cehreli, Z. N., and Yavuz, I., 2005. "Index of Resolution Quality for Large Eddy Simulations". *Journal of Fluids Engineering,* **127**(5), pp. 949–958.

[27] Yahou, T., Schuller, T., and Dawson, J. R., 2023. "Analysis of the ignition dynamics of h2-enriched premixed flames using high speed piv/oh-plif". *Proceedings of the European Combustion Meeting*.